Biophysical Journal Volume 71 October 1996 1680–1694

Kinematics of Red Cell Aspiration by Fluorescence-Imaged Microdeformation

Dennis E. Discher*#§ and Narla Mohandas#§

*Department of Physics, Simon Fraser University, Burnaby, BC V5A 156 Canada, #Life Sciences Division, Lawrence Berkeley Laboratory, University of California, Berkeley, California 94720, and the §Joint Graduate Group in Bioengineering, University of California, Berkeley and San Francisco, California 94143 USA

ABSTRACT Maps of fluorescing red cell membrane components on a pipette-aspirated projection are quantitated in an effort to elucidate and unify the heterogeneous kinematics of deformation. Transient gradients of diffusing fluorescent lipid first demonstrate the fluidity of an otherwise uniform-density bilayer and corroborate a "universal" calibration scale for relative surface density. A steep but smooth and stable gradient in the densities of the skeleton components spectrin, actin, and protein 4.1 is used to estimate large elastic strains along the aspirated skeleton. The deformation fields are argued to be an unhindered response to loading in the surface normal direction. Density maps intermediate to those of the compressible skeleton and fluid bilayer are exhibited by particular transmembrane proteins (e.g., Band 3) and yield estimates for the skeleton-connected fractions. Such connected proteins appear to occupy a significant proportion of the undeformed membrane surface and can lead to steric exclusion of unconnected integral membrane proteins from regions of network condensation. Consistent with membrane repatterning kinematics in reversible deformation, final vesiculation of the projection tip produces a cell fragment concentrated in freely diffusing proteins but depleted of skeleton.

INTRODUCTION

The collective movements of a cell's various lipid, protein, and carbohydrate constituents define the component kinematics of a cell in motion or deformation. Toward obtaining a direct view of cellular component kinematics during a controlled deformation, a micropipette method of fluorescence-imaged microdeformation (FIMD) has recently been developed and applied to the highly deformable red cell (Discher et al., 1994). Here we elaborate on, quantify, and present minimal interpretations of some of the key static and dynamic aspects of constituent kinematics in red cell aspiration.

The two main structural components of the red cell membrane are often considered to be the lipid bilayer, with its embedded proteins, and a peripheral skeletal network of spectrin, actin, and protein 4.1 (surfaces S_2 and S_1 in Fig. 1, respectively). Cohesiveness of the lipid bilayer confers a strong resistance to cell area changes in extreme pressurization of the erythrocyte (Evans and Skalak, 1980; Katnik and Waugh, 1990). A shear elasticity of the membrane has long been held to arise from the underlying skeletal network (Evans and Skalak, 1980; Hochmuth, 1987; Mohandas and Evans, 1994), whereas a distinct compressibility of the network was, for many years, only a matter of speculation (Stokke et al., 1986; Kozlov and Markin, 1990). The membrane network is a highly organized mesh of the long, filamentous protein spectrin: spectrin cross-links small junctional complexes containing short actin filaments (Byers and Branton, 1985), and spectrin-actin interactions are stabilized by protein 4.1. Attachment of the skeleton to the bilayer appears to primarily involve the abundant transmembrane proteins Band 3 and glycophorins. Additional integral membrane proteins fulfill various other functions. CD59, for instance, is a glycosyl-phosphatidylinositol (GPI)-anchored protein of low surface density (in surface S_3 of Fig. 1) that is known to inhibit complement-mediated lysis of the red cell (Test and Woolworth, 1994). Many of the red cell proteins, the structures they assemble into, and the functions they serve have important roles in other tissues (Goodman et al., 1988). Many of these proteins are also found to be highly conserved through evolution (e.g., Debreuil et al., 1987). Relationships between the components of the red cell membrane and mechanical function are therefore expected to be of broad biological significance.

The physical behavior of molecules within the membrane is certainly heterogeneous. Molecular mobility in diffusion is, as a central example, highly dependent on the particular membrane component studied. Fluorescence recovery after photobleaching (FRAP) shows in particular that somewhat less than half of Band 3 in the red cell membrane is mobile on short time scales (<30 min). Moreover, diffusivity of the mobile Band 3 is about two orders of magnitude smaller than that of lipid bilayer probes which exhibit nearly 100% mobility (Golan and Veatch, 1980; Golan et al., 1984; Tsuji and Ohnishi, 1986). These results seem consistent with the view that a significant fraction of Band 3 molecules (with cell-average density of $\sim 10^4/\mu m^2$) are involved in connecting the underlying, solid-like skeleton to the bilayer, and with the view that the lipid bilayer is fluid in its surface. In contrast to Band 3, GPI-linked proteins on a variety of other cell membranes appear more mobile: typical mobile fractions are $\sim 75 \pm 10\%$, and diffusivities of GPI-linked pro-

Received for publication 5 January 1996 and in final form 10 July 1996.

Address reprint requests to Dr. Dennis Discher, University of Pennsylvania, 297 Towne Bldg, Philadelphia, PA 19104-6315. Tel.: 215-898-8342; Fax: 215-573-6334; E-mail: discher@eniac.seas.upenn.edu.

0006-3495/96/10/1680/15 $2.00

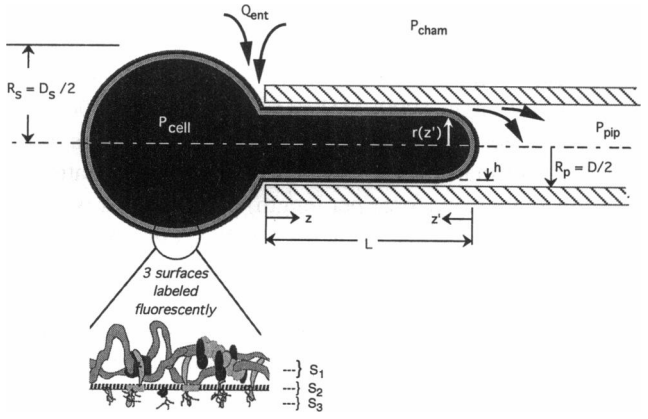

FIGURE 1 Schematic of a red cell aspirated into a micropipette ($R_p \approx$ 0.5 to 1 μm). A hydrostatic pressure, P_{cell}, builds up within the cell, leading to a membrane tension that smooths the cell contour. A magnified view of the red cell membrane shows it as a trilaminate of S_1, an internal skeletal network of proteins; S_2, the lipid bilayer; and S_3, an exofacial layer of integral proteins and integral protein domains. In this idealization, a line normal to one surface is normal to the other two surfaces. Specific components of each surface were fluorescently labeled, and their distributions were imaged. Dimensionless projection length L/R_p is controlled primarily by osmotic adjustment of cell volume (160–250 mOsm). A pressure difference, $P_{cham} - P_{pip}$, between the pipette and the external chamber solutions (phosphate-buffered saline with 30–50% autologous plasma or albumin at 5–15 mg/ml) produces a small flow into the pipette.

teins approach half those of lipid probes (Noda et al., 1987; Zhang et al., 1991). Some impedance to diffusive motion of these mobile proteins has been attributed to exofacial structures (Zhang et al., 1991); steric interactions between mobile integral membrane proteins and immobile proteins, perhaps skeleton-connected, have previously been quantitated in terms of cell surface area occupied by the immobile proteins (Ryan et al., 1988). Diversity in the "thermal" mobility of membrane species certainly potentiates a similar level of complexity in directed, collective motions of specific components during controlled membrane deformation.

Employing many of the fluorescent labeling strategies of FRAP along with a reversible hemolysis technique that permits labeling of the internal skeleton, fluorescence microscopic imaging was used to map out the constituent density fields of a controllably deformed portion of red cell membrane (Fig. 1). We present here results and analyses complementary to those that recently appeared in a brief, introductory report (Discher et al., 1994). Calibration of intensity maps is elaborated first as a means of providing the basic physical quantity of FIMD: the relative surface density field of a component. Fluidity of the lipid bilayer is made explicit, and a surface diffusion constant for lipid is calculated from transient gradients in diffusing fluorescent lipid probe. The peripheral skeletal network components spectrin, actin, and protein 4.1 are all shown to reveal a single solid-like network in dilation at the tip of the membrane projection but in compression at the pipette entrance. The smooth, almost linear gradient in network density is later used to elucidate large elastic strains in the network. Integrations of the various relative density fields together with direct measures of the effective gap between the membrane and the pipette all suggest that the deformation fields in membrane aspiration are an unhindered response to loading in the surface normal direction. Density maps intermediate to those of the compressible skeleton and fluid bilayer are exhibited by the transmembrane protein Band 3, yielding simple estimates for the skeleton-connected fraction of Band 3. The physical bulk of this protein and other connected proteins would appear to occupy a significant proportion of the undeformed membrane surface area. Such a proportion can be estimated from the measured exclusion of unconnected integral membrane proteins from the pipette entrance and the measured enrichment of these same mobile proteins at the projection tip. The redistribution of components apparent in membrane vesiculation is illustrated as an immediate consequence of kinematics within the reversible regime of membrane deformation. In sum, quantitative kinematics and simple, unifying analyses are thus developed, based on fluorescence-imaged microdeformation of the red cell.

MATERIALS AND METHODS

Table 1 summarizes the strategies employed in fluorescently labeling components of the red cell membrane. Some of the details on the materials and methods have been given elsewhere (Discher et al., 1994, 1995). The purity of all Fabs was verified, and antibody was ultracentrifuged before use to remove aggregates.

To label the internal skeletal network, red cells were reversibly permeabilized by cold, hypotonic lysis, allowing fluorescent probes in the lysis buffer to diffuse into the cell "ghost" and bind (Takakuwa et al., 1986; Discher et al., 1995). Mechanical properties of the resealed membrane were not altered by the labeling procedure as evaluated by both micropipette aspiration and ektacytometry. A concentration-dependent edge brightness with rhodamine-phalloidin indicated an apparent, in situ $K_a \approx 3 \times 10^6$ M^{-1} (Discher et al., 1995), slightly less than in in vitro assays. None of the protein solutions were able to fluorescently label unlysed cells. Incorporation of protein 4.1 or a recombinant spectrin-actin binding domain has been shown to normalize the mechanical strength of protein 4.1-deficient membranes (Takakuwa et al., 1986; Discher et al., 1995). Ektacytometry has shown that anti-spectrin Fabs do not alter membrane deformability (Nakashima and Beutler, 1978).

TABLE 1 Membrane component labeling strategies

Labeled surface	Labeled component	Labeling methodology*
S_1:network	Spectrin	FITC-polyclonal Fab to αII46 domain
	Actin	rhodamine or fluorescein phalloidin
	Protein 4.1	FITC-4.1 in 4.1-deficient cells
S_2:lipid bilayer	Phospholipid	FL-PE
	Synthetic	diO
S_3:integral proteins	Band 3	ema, fma, or FITC-monoclonal Fab
	Glycophorin C	FITC-monoclonal Fab or IgG
	CD59	rhodamine monoclonal Fab
	Anti-FL-PE	Texas Red IgG

*See Materials and Methods for additional details. FITC, Fluorescein isothiocyanate; Fab, antibody fragment; FL-PE, fluorescein phosphatidylethanolamine; diO, 1,1'-dihexadecyloxacarbocyanine; ema, eosin-5-maleimide; fma, fluorescein-5-maleimide.

Fluorescent dextrans were dissolved in phosphate-buffered saline, filtered, and ultracentrifuged to remove aggregates.

The micropipette system is based upon previous descriptions (Evans, 1989; Discher et al., 1994). Briefly, a conventional Nikon Diaphot was outfitted with a standard video camera and with a liquid nitrogen-cooled CCD camera (CH-260; Photometrics, Tucson, CA) for accurate quantitation of very low-level fluorescence (Hiraoka et al., 1987). To collect light from the full depth of the fluorescing membrane cylinder, an objective lens with a depth of focus on the order of the pipette diameter was used (Zeiss Neofluar 40×, 0.75 NA). Similar images were obtained with both higher power and lower power objectives. A very limited amount of imaging was also done with the confocal microscope at the Microscopy Center at UC Berkeley. The interval of aspiration to the deformed state was varied from <1 s up to 5 min, and image collection ranged from 100 ms to 10 s; neither variable had a discernible effect. In addition, cells could be aspirated reversibly a number of times under bright-field illumination before fluorescence imaging; however, prolonged excitation of fluorescence invariably led to some photofixation. This could be demonstrated by expelling the cell and observing that it partially retained its aspirated form.

Kinematic preliminaries

As the differential geometry of curved surfaces is made use of in the analyses, a brief overview of some preferred notation is given (Naghdi, 1972; Evans and Skalak, 1980; Naghdi and Vongsarnpigoon, 1985). On an arbitrary surface, S_n, of density ρ (mass or molecules per area) with material coordinates given by (θ_1,θ_2) and spatial position specified by the vector components $r_i(\theta_1,\theta_2)$ $(i = 1, 2, 3)$, a measurement of distance between any two points of the surface, indeed any geometric quantity, can be obtained from a metric tensor with components $a_{\alpha\beta} = (\partial r_i/\partial\theta_\alpha)(\partial r_i/\partial\theta_\beta)$ $(\alpha, \beta = 1, 2)$ for the surface. Relative to a reference state having metric components $A_{\alpha\beta}$ and initial surface density ρ_o, a relative surface density $\bar{\rho} = \rho/\rho_o$ is given by $[\det(a_{\alpha\beta})/\det(A_{\gamma\delta})]^{1/2}$. This is a local form for conservation of mass. The curvature tensor may also be obtained from the metric; the principal radii of curvature, R_1 and R_2, are given by the eigenvalues of the curvature tensor. On the tip of the aspirated projection, $R_1 = R_2 = R_p$; along the cylindrical portion, one of these radii goes to ∞.

The overall shape and surface density field together constitute a geometric description that is kinematically complete for static equilibrium of a surface fluid. However, in the case of an axisymmetric, solid surface deformed (without torsion) to another axisymmetric, solid surface, the kinematics may be developed further. Basis vectors tangent to the lines of curvature on each surface diagonalize the metric tensors, i.e., $a_{12} = a_{21} = A_{12} = A_{21} = 0$. Relative to the initial or reference surface, the nonzero metric components, or eigenvalues, can be shown to be the squares of the extension ratios along the lines of curvature; as continuous functions of position, the extension ratios or stretches are denoted λ_1 and λ_2, where, for example, $\lambda_1^2 = a_{11}/A_{11}$. As the metric tensor completely specifies the geometric state of the surface, the shape change and all kinematic quantities for this axisymmetric elastic surface are fully prescribed by these two degrees of freedom on the surface, λ_1 and λ_2. In particular, the local form for conservation of mass defines a relative surface density $\bar{\rho} = \rho/\rho_o = 1/(\lambda_1\lambda_2)$. Conversely, given the axisymmetric shapes (i.e., curvatures) of the reference and deformed surfaces and noting that $\lambda_1 = \lambda_2 = 1/\sqrt{\bar{\rho}}$ at those points lying on the axis of symmetry, integral forms for the conservation of mass will allow a determination of the stretch fields from the relative surface density. Explicit use will be made of this ability to obtain stretch or strain information from a solid surface's density field.

RESULTS

Aspiration and fluorescence imaging

Upon initial aspiration of a flaccid cell (wherein $P_{cell} \approx P_{cham} > P_{pip}$), a small projection of membrane enters the micropipette. Eventually, as the cell becomes pressurized ($P_{cell} > P_{cham}$), continued aspiration is strongly resisted and an optically smooth membrane contour results (sketched in Fig. 1). It is commonly accepted (Evans and Skalak, 1980; Katnik and Waugh, 1990; Mohandas and Evans, 1994) that this is a state maintained by purely normal loads (i.e., pressures), primarily on the bilayer, and that the statically determinate tension (force per length) in the bilayer is given by $T = \frac{1}{2}(P_{cham} - P_{pip})R_sR_p/(R_s - R_p)$. For our studies, $(P_{cham} - P_{pip}) \approx 20$ kdyn/cm^2 should thus produce a nominal tension in the bilayer of ~1 dyn/cm. This tension is ~10% of that required for cell lysis (Evans and Skalak, 1980), and, based on numerous constitutive assumptions (including surface isotropy), this level of bilayer tension can be associated with a uniform surface dilation of only ~1%, i.e., lipid density changes are minimal in cell aspiration.

Subsequent to the aspiration of a homogeneously fluorescent cell or cell ghost into the pipette, an image of the aspirated form is collected. Representative intensity maps (Fig. 2) illustrate the common features of axisymmetry and relatively uniform fluorescence emanating from the spherical portion of membrane held outside the pipette. Quantitation of the variations around this "crown" typically indicate less than 10% spatial variation for the highest intensity images. Close to the pipette's entrance edge, diffraction may add anomalously to the variation.

Three basic types of nearly monotonic response appear along the length of the projection. The lipid bilayer probe fluorescein phosphatidylethanolamine (FL-PE) uniformly covers the projection (Fig. 2 *A*). The skeletal actin probe rhodamine phalloidin gives a signal decreasing almost linearly toward the tip (Fig. 2 *B*). Finally, a rhodamine-tagged antibody to the GPI-linked receptor CD59 gives a signal that is increased at the tip (Fig. 2 *C*), in marked contrast to the actin. These three distinct responses suggest that the images obtained truly reflect molecular redistribution over the sphere-cylinder-cap geometry rather than a systematic artifact of the FIMD methodology. Further evidence will clarify the kinematic meaning of these responses. Additional results will also attempt to establish the nature of the aspiration forces that lead to the various membrane responses.

Lipid bilayer statics and a density scale

It is first necessary to point out that convolution of fluorophore distributions through the imaging optics could present obstacles to obtaining accurate density maps from the intensity distributions. However, with the lipid bilayer labeling, the uniformity of edge brightness along the image of the sphere as well as along the cylinder indicates a homogeneous density of lipid that is common to both the sphere and the capped cylinder. For the cylinder, this assertion can be made more rigorous by a straightforward analysis of the image. Integration of pixel intensities across the width of the imaged projection gives the profile illustrated in Fig. 3 (in bold). The formation of the image essentially involves op-

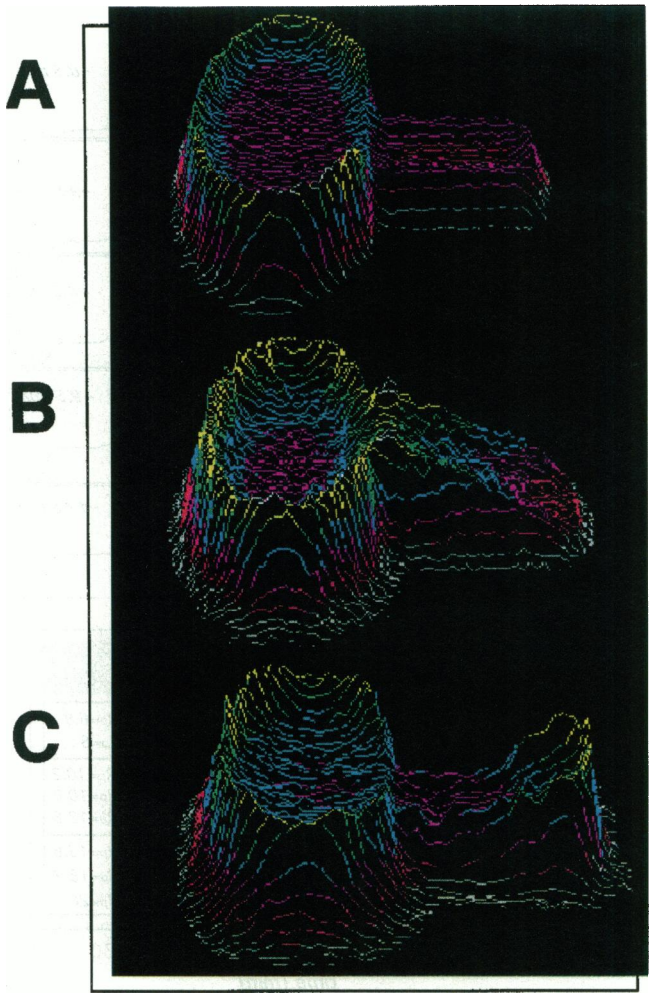

FIGURE 2 Intensity maps for specifically labeled components of the red cell membrane. The raw intensity data were gathered through conventional optics and are shown without deconvolution. (*A*) Lipid bilayer probe FL-PE. (*B*) Skeletal network probe to actin, rhodamine phalloidin. (*C*) Exofacial layer probe to GPI-linked CD59: rhodamine-labeled monoclonal Fab. Note the axisymmetry and the uniformity of intensity emanating from the spherical contour.

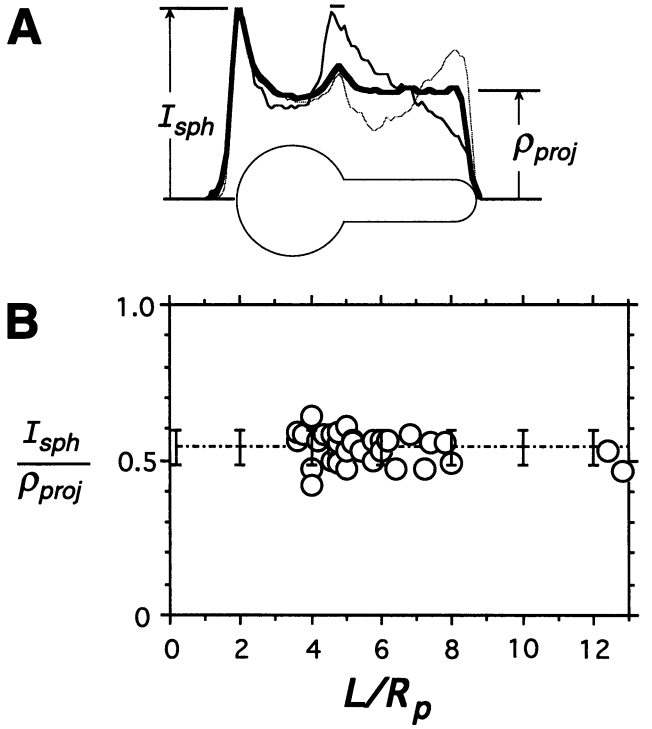

FIGURE 3 (*A*) Integrated intensity sections for lipid (*heavy line*), actin (*line*), and CD59 (*broken line*), as obtained by summation of pixel intensities across a strip of width $2R_p$ bracketing the aspirated projection. (*B*) Lipid probe results. Data represent 50 different aspirated cells. The ratio of midpoint density ρ_{proj} to integrated intensity from the sphere I_{sph} appears to be independent of aspirated projection length, L/R_p. This provides a method for calibration.

tical "integration" in the direction normal to the object and image planes. Thus, for the cylinder of membrane, the integrated intensity profile represents a line density (mass per length) of fluorophore. The integration profile may also be shown to be the line density along the symmetry axis of the cap (Appendix 1), and therefore, given the axisymmetry, the projection's line density $\tilde{\lambda}_{proj}$ also reveals the lipid's surface density (as a mass per area). This argument is easily extended to an axisymmetric but nonhomogeneous cylinder of membrane. For the lipid then, the flatness of the integrated intensity profile clearly indicates a uniform surface density, designated ρ_{proj}, over the entire projection, including the hemispherical cap.

The largest peak on the integrated intensity profile originates from the diffraction-limited image of a portion of the sphere antipodal to the aspirated projection. The magnitude, I_{sph}, of this peak depends only weakly on the radius of the sphere because of the thinness of the membrane; a simple projection-attenuation model of image formation leads to a $\sqrt{R_s}$ dependence. Over a broader range of labeling concentrations and a fair range of both pipette diameters and sphere sizes, it was found that I_{sph}/ρ_{proj} was nearly constant ($I_{sph}/\rho_{proj} = 1.85 \pm 0.17$ for 50 images of 50 cells). Aspiration pressures ranging from 5 to 50 kdyn/cm^2 gave values for this ratio within the scatter of the data. The results therefore imply that the relative surface density $\bar{\rho}_{lipid} = (\rho/\rho_o)_{lipid} = 1.0$ within a few percent. The lipid results thus provided the measure of 1 on a scale for converting all fluorescing component images to relative surface density profiles. It may be noted that the empirically derived ratio $(I_{sph}/\rho_{proj})_{lipid}$ primarily reflects the difference in imaging a sphere and cylinder of equal and uniform surface density. Additionally, if I is the edge intensity of the sphere (i.e., crown height in Fig. 2 *A*), I_{sph}/ρ_{proj} of Fig. 3 is proportional to $2R_pI$ scaled by $2\pi R_p\tilde{\lambda}_{proj}$.

Confocal images of cells brightly labeled with the lipophillic probe 1,1′-dihexadecyloxacarbocyanine tended to support the above interpretation of images obtained by conventional microscopy. With confocal microscopy, out-of-focus light was reduced as an optical slice was taken through the midsection of the cell. The signal-to-noise ratio from the confocal system was about two to three times less than that obtained with the conventional microscope, but a

fairly flat response on the membrane cylinder was still obvious. Confocal microscopy gave $I_{sph}/\rho_{proj} = 0.96 \pm 0.08$ (four cells); a value very close to unity was to be expected, as the micropipette had a diameter somewhat larger than the depth of the confocal slice. With more depth to the sphere than the cylinder (i.e., $R_s > R_p$), conventional microscopy was expected to yield a value for I_{sph}/ρ_{proj} greater than 1, as found.

Lipid diffusion in the bilayer

A slight modification of the standard micromanipulation chamber allowed fluorescence labeling of an already aspirated cell. A reservoir of fluorophore was connected by a narrow channel to the manipulation chamber. Unlabeled cells were aspirated and translated from an observation zone at the opposite end of the chamber into a labeling zone near the mouth of the channel. After 1 to 2 min of labeling, the cell was translated back for observation.

One set of such transfer experiments involved lipid probe labeling of just the spherical portion of cell membrane outside the micropipette. This outer contour could then, in principle, act as a surface reservoir to drive lateral diffusion onto the aspirated membrane projection. The relative size of the spherical reservoir, $(D_s/2R_p)^2/(L/2R_p)$, ranged between a value of 1 and 3.4. After labeling of the cell membrane outside the pipette, sequential imaging (Fig. 4 *A*) of fluorophore motion down the unlabeled membrane projection clearly demonstrated that a gradient in a lipid could be obtained, although in this case it could not be sustained over time. Several minutes were required for the self-diffusion of lipid to achieve an equilibrium distribution wherein the relative surface density of labeled lipid at the cap approached 1 (Fig. 4 *B* and Table 2). This same state is observed "instantaneously" upon aspiration of a prelabeled cell. The large difference in time scales suggests that, under the forces of membrane aspiration, in-plane motions of lipid are being directed rather than being strictly diffusive.

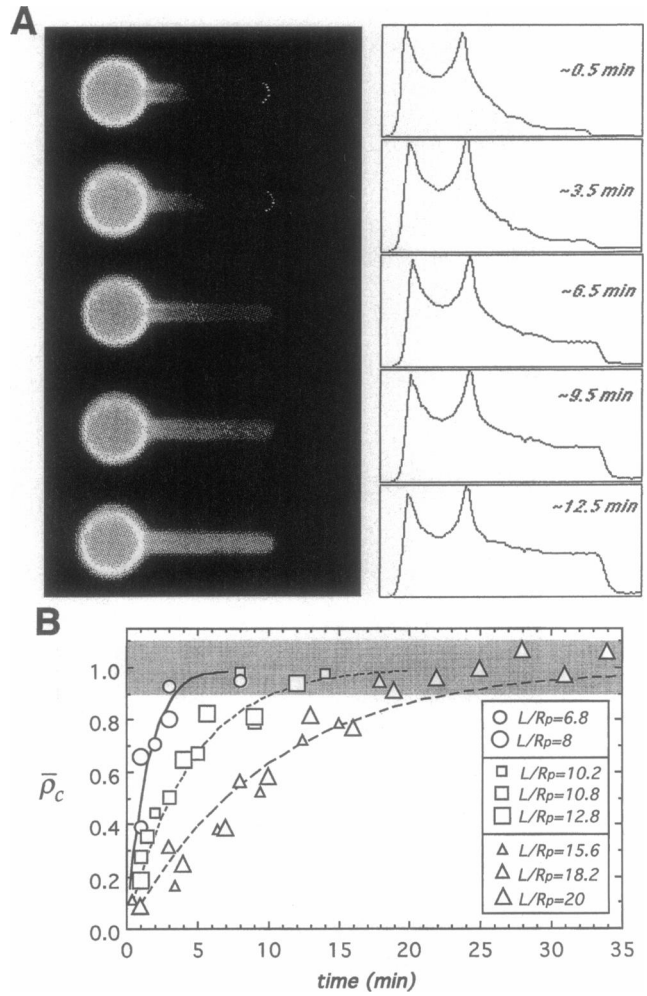

FIGURE 4 (*A*) Evolution of lipid probe (FL-PE) on a projection after postaspiration labeling. Compare the end-point intensity section (at 12.5 min) with the lipid results of Figs. 2 and 3. The latter were obtained with cells labeled before rather than after aspiration. (*B*) Relative surface density of lipid probe at projection cap, $\bar{\rho}_c$, plotted against evolution time. Exponential fits for the three groupings of data are listed in Table 2.

Protein network kinematics

In stark contrast to the static lipid result, the network exhibits a strong, roughly linear gradient in density along the cylindrical projection (Fig. 2 *B*): network density is high at the pipette entrance and low at the tip or cap of the membrane projection. However, the density appears nearly uniform over most of the sphere, and so it was assumed that the relative surface density on the part of the sphere antipodal to the pipette is essentially 1 ($\pm 10\%$). Given this and the empirically derived ratio $(I_{sph}/\rho_{proj})_{lipid}$, the integrated intensity profiles of the network constituents on the projection were quantitated as relative surface density profiles. By this scheme, network spectrin, actin (Discher et al., 1994), and protein 4.1 all show compression at the pipette entrance ($\bar{\rho}_e > 1$) and dilation at the projection's cap ($\bar{\rho}_c < 1$) (Fig. 5 *A*). Specifically, rhodamine- or fluorescein-phalloidin labeling of actin and fluoresceinated Fabs against α-spectrin all showed this form of graded response on the projection pulled from ghost membranes of normal cells. Fluoresceinated protein 4.1 incorporated into protein 4.1-deficient ghosts showed a similar gradient in projection density. This seems consistent with previous conclusions that the membranes of protein 4.1-deficient cells have near-normal elastic properties (Waugh, 1983). In addition to experiments with purified protein 4.1, the steep gradient was also found after incorporating a recombinant, fluorescently labeled spectrin-actin binding domain of protein 4.1 (Discher et al., 1995).

The 4.1-deficient cells are also notable for their highly ellipsoidal shape. It was found that aspiration of a 4.1-deficient cell in a direction parallel to its major axis resulted in very little gradient. This contrasted with the results for protein 4.1 in Fig. 5, wherein aspiration was done in regions

TABLE 2 Diffusion of lipid probe onto an aspirated projection of membrane

L/R_p	D_s/R_p	R_p (μm)*	$\sim\tau$ (s)#	D_{lipid} (cm^2/s)
8.0	7.4	0.59	210	0.7×10^{-9}
10.2	6.8	0.66	270	1.1×10^{-9}
10.8	8.2	0.50	270	0.8×10^{-9}
12.8	7.4	0.56	270	1.3×10^{-9}
15.4§	5.8	0.65	600	1.2×10^{-9}
15.6	7.0	0.54	600	0.9×10^{-9}
18.2	6.0	0.64	600	1.6×10^{-9}

*The pipette radius was calculated by first assuming the ensemble had an average cell area of $\langle A \rangle = 135\ \mu m^2$ (Fung, 1993), a value with a typical standard deviation of about $\pm$ 10%, and then using $R_p^2 = (\alpha\langle A\rangle/4\pi)/[L/2R_p + (D_s/2R_p)^2]$, where α is the area of a cell divided by $\langle A\rangle$. The pipette radius was estimated in this manner because a somewhat coarser than usual spatial pixelation during image collection was required to increase the sensitivity and allow multiple images to be collected with minimal photobleaching.

#Time constants determined from the data of Fig. 4.

§A fold in the projection at the pipette entrance was apparent after labeling. This entrance region was heavily labeled by the time observation began; it was therefore subtracted to reduce the projection length from $L/R_p = 20$.

distant from the major axis. However, the flattened response along the ellipsoid's major axis is consistent with 1) the expectation of a minimal network deformation for a minimal cell distortion in this case and 2) minimal adhesion to the pipette or obstruction by the pipette in the formation of gradients on normal cells.

Because the cell ghosts used in these network studies were resealed, several of the affinity probes to the internal cytoskeleton also showed significant fluorescence entrapped within the cell. The effect in imaging such cytoplasmic fluorophore was simulated by fluorescent dextrans or albumin. These inert fluorophores showed that the dominant effect is a filling in of the crowns pictured in Fig. 2. This reflects the fact that the sphere has an imaged depth ($\sim D_s$) several times that of the cylinder ($\sim 2R_p$). As the entrapped albumin and dextrans also gave a flat response on the projection, the difference between the entrance and cap densities of the network (Fig. 5 *B*) should be expected to give a very accurate measure of the network gradient. However, to maximize the bound-to-free ratio of the probe, and thereby minimize the volumetric signal from free probe, 1) a low probe concentration was used, and/or 2) free probe was washed out before resealing, in an effort to kinetically trap bound probe.

To address the possibility of artifacts in interpretation that might be attributable to the ghost formation process, subtle geometric variations, and the density calibration scheme, double-label experiments were performed in which cells were labeled with both FL-PE and rhodamine-phalloidin. Separate fluorescence images were taken, one after the other, and in subsequent analyses the lipid result for each ghost was used for calibrating that ghost's actin profile. These results from double-labeling fell within the scatter of Fig. 5 *B*.

Holding the aspirated cells in the micropipette for 10 or 30 min gave a gradient well within the scatter of the gradients observed immediately after aspiration (Fig. 5 *C*). Sustained deformation of the network thus does not lead to detectable relaxation. This is consistent with a highly elastic but very stable network. These findings, together with the broad range of affinity labels employed (K_a ranging from $\sim 10^5$ to $\sim 10^8$ M^{-1}), and the overall consistency, albeit scatter, in the trends of Fig. 5 minimize possible concerns for stress dependence in the noncovalent probe associations.

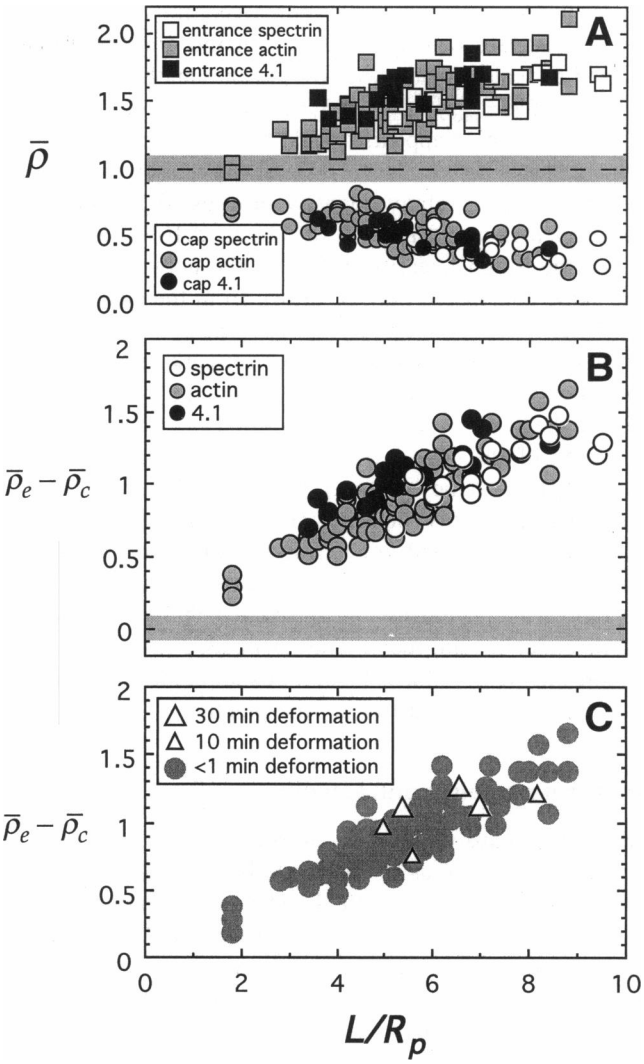

FIGURE 5 (*A*) The three primary network components' relative apparent surface densities at the pipette entrance, $\bar{\rho}_e$, or projection cap, $\bar{\rho}_c$, are shown as divergent functions of membrane projection length. The data represents ~100 individual cell ghost membrane projections, which had been aspirated in more than 10 different experiments. The gray region denotes the uncertainty in any particular measure due to the variance in the lipid calibration scale. The gray region centered at zero in *B* indicates, for lipid, the range of difference in $\bar{\rho}_e$ and $\bar{\rho}_c$. (*C*) Cells were held in the pipette for an extended time and then imaged. No significant relaxation was found.

Numerical integrations of the measured relative density profiles on the projection indicate that the elevated density of network material at the pipette entrance, $\bar{\rho}_e$, is not an anomalous accumulation or pipette edge effect. First, because the relative surface density of lipid, $\bar{\rho}_{lipid}$, is 1 to 1.01

under the aspiration pressures employed, the integral of the relative surface density of lipid over the projection is expected to scale linearly with projection length (Fig. 6), i.e., $_{proj}\int \bar{\rho}_{lipid}\, da \approx {}_{proj}\int da = 2\pi R_p(L - R_p) + 2\pi R_p^2 = 2\pi R_p L$. The same relation appears to hold for the aspirated network, i.e., $_{proj}\int \bar{\rho}_{net}\, da \approx 2\pi R_p L$, based on the integration of several network relative density profiles, $\bar{\rho}_{net}$, and within experimental uncertainties of about ±10%. Moreover, given the rough linearity typical of the network gradients, the same conclusion may be drawn from the data in Fig. 5 *A*, which yield in calculation $\frac{1}{2}(\bar{\rho}_e + \bar{\rho}_c)_{net} = 1.02 \pm 0.11$ (±SD). In other words, the ratio of network-to-lipid surface densities of the initial cell ($\rho_{o,\,net}/\rho_{o,\,lipid}$ = constant) is nearly the same as the network-to-lipid ratio averaged over the area of the final aspirated projection ($_{proj}\int(\rho_{net}/\rho_{lipid})\, da/_{proj}\int da$ = same constant). These simple integrations of the relative density fields imply that the network is not significantly impeded in entering the pipette during aspiration. Gradients in network components are therefore likely to represent the intrinsic mechanical behavior of the network under loading conditions associated more with aspiration and pressure loads than, for example, with component adhesion to or obstruction by the pipette.

Integral protein connectivity

Molecular maps of Band 3 showed a gradient response in the same direction as the network, but of lesser magnitude (Fig. 7 *A*) (Discher et al., 1994). The ratio of entrance to cap density of Band 3 increased with projection length and was insensitive to the reversible hemolysis used in obtaining the cell ghosts. This lack of difference between intact red cells and resealed cell ghosts indicates a minimal effect of the ghosting process on membrane mechanics. In addition to affinity labeling of Band 3 with a fluoresceinated monoclonal antibody fragment, both eosin and fluorescein maleimides were covalently bound to Band 3, and the eosin fluorescence was quantitated through both fluorescein and rhodamine filter sets. The fluorescein probes allowed double labeling with rhodamine phalloidin and thereby demonstrated most convincingly that the redistribution of Band 3 in aspiration does not map directly onto the reorganized skeleton of normal cells. Instead, the gradient response in Band 3 was consistently shallower than the gradient in actin. For a particular projection length, Band 3 density tended to be higher than actin density at the cap of the membrane projection, hence $(\bar{\rho}_e/\bar{\rho}_c)_{Band3}$ is between that of actin and lipid. Simple fits of the data illustrated in Fig. 7 *A* capture these differences in gradients most succinctly (Table 3). A plausible mechanism for the relative increase of Band 3 at the cap would seem to be the in-surface convection of a Band 3 mobile fraction with lipid during the process of aspiration.

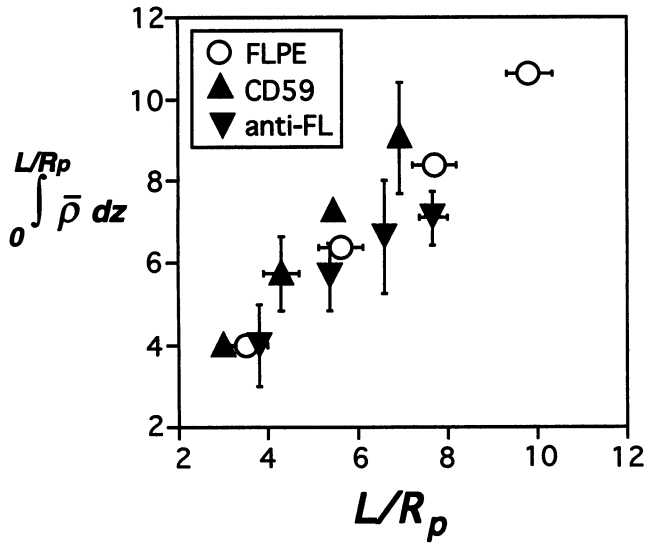

FIGURE 6 Relative surface mass on the projection as an integral of the relative surface density is shown to be an increasing function of projection length for lipid, CD59, and the lipid-linked antibody. Binned data have been averaged as indicated.

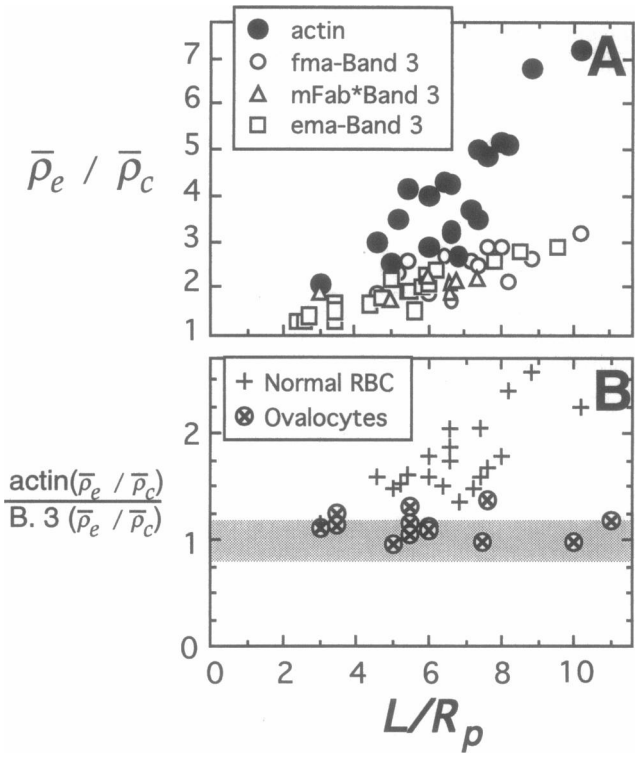

FIGURE 7 Comparison of entrance over cap density ratios for Band 3 and actin in normal and pathological red cells. (*A*) Different strategies of labeling Band 3 all reveal a shallower gradient in Band 3 compared to the network. Results with the two Band 3 labels fluorescein-5-maleimide (fma) and fluorescein isothiocyanate–monoclonal Fab include cell ghosts that were also labeled with rhodamine phalloidin. (*B*) In contrast to the normal cell membranes, Band 3 on abnormal, ovalocytic red cells gives an entrance to cap density ratio comparable to that of actin and consistent with reports of restricted mobility of the Band 3. Band 3 and actin in the same cell were again both labeled, and the region in gray indicates the maximum range of variation seen with control membranes double-labeled for actin with both fluorescein and rhodamine phalloidin.

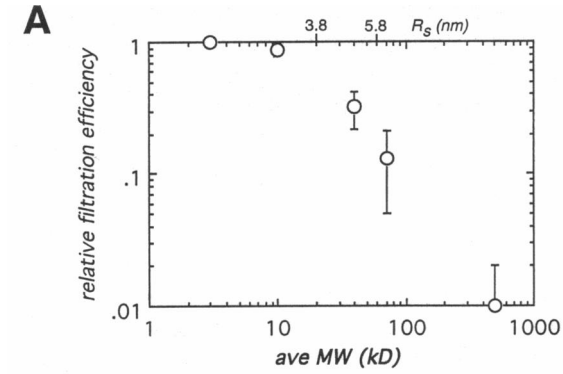

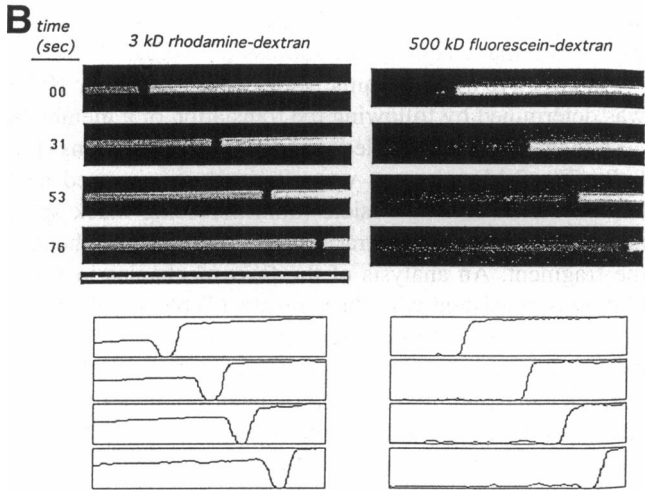

FIGURE 8 (*A*) Converging flow of medium into the gap between cell and pipette can convect fluorescent dextrans into the pipette volume. The filtration efficiency of various fluorescein dextrans relative to a 3-kDa rhodamine dextran when allowed to simultaneously leak past an aspirated cell ($L/R_p \approx 6$–10). The top axis gives the Stokes radius, R_s, for dextrans in the critical range of molecular weights ($MW_n \equiv$ number average) (Laurent and Granath, 1967). (*B*) Motion of a cell fragment up the pipette observed as a black spot against fluorescent dextrans (3 kDa and 500 kDa) already in the pipette. Scale bar is 2 μm per division. The remainder of the aspirated cell still occupies the pipette entrance ~4 μm to the left. The corresponding integrated intensity profiles show minimal gradients in fluorescence within the pipette. The fragmentation was induced by the application of higher aspiration pressure, which was quickly returned to 20 kdyn/cm^2.

The validity of double labeling was also established in cell ghosts labeled simultaneously with both fluorescein phalloidin and rhodamine phalloidin. The ratio of entrance to cap densities for the fluorescein phalloidin signal was always within ±15% of the signal from the rhodamine phalloidin. This range is small compared to the apparently exponential increasing difference between actin and Band 3 (Fig. 7 *B*) on normal cells.

The distinction above between Band 3 and actin was further substantiated by a set of studies on abnormal red cells (southeast Asian ovalocytes or SAOs) in which the mobile fraction of Band 3 had previously been shown by FRAP to be reduced to ~5 ± 5% (Mohandas et al., 1992). A reduced ability to separate Band 3 from detergent-treated skeletons of SAO cells (Moriyama et al., 1992) suggested a tighter association, of an unknown nature, between Band 3 and the skeleton in SAO cells. FIMD results with SAO cells support this proposition, because there appeared to be little difference between Band 3 and actin at either the projection cap or the pipette entrance (Fig. 7 *B*). Of added interest is the observation that the limited data on SAO actin gradients fell within the scatter of normal cells (e.g., Fig. 5).

In contrast to the decrease in the density of network-connected proteins at the projection tip, the GPI-linked protein CD59 (Fab-labeled) was found to be enriched at the tip of the membrane projection (Fig. 2 *C*). The amount of CD59 enrichment at the cap was found to increase with the length of membrane projected into the pipette (Table 3 and Discher et al., 1994). As found with the network, however, the total amount of CD59 on the projection was approximately the same as the amount of lipid, $_{proj}\int\bar{\rho}_{CD59}\,da \approx {}_{proj}\int\bar{\rho}_{lipid}\,da$ (Fig. 6). Like the network, then, CD59 does not appear to be significantly impeded in entering the pipette.

The negative exponent or slope in the CD59 response was typical of a larger class of unconnected integral membrane proteins (Table 3). This class included a Texas Red conjugated anti-fluorescein IgG assembled onto the outer surface of the red cell via the headgroup fluorescein of FL-PE. The apparent density of antibody at the cap increased with aspiration. In addition and again consistent with minimal impediment to surface transport at the pipette entrance, the integrated relative density of protein on the projection tended to increase in parallel with the amount of lipid on the

TABLE 3 Two empirical fits* of $\bar{\rho}_e/\bar{\rho}_c$

Component	γ in exp [$\gamma(L/R_p)$]	γ in [1 + $\gamma(L/R_p)$]
Actin	+0.21	+0.55
Gly C (normal cells)	+0.18	
Band 3	+0.13	+0.30
Lipid	0.0	0.0
Anti-FL on FL-PE	−0.10	−0.24
CD59	−0.12	
Gly C (4.1-cells)	−0.15	−0.37

*The use of two simple fits serves to emphasize that no modeling is being done here toward predicting functional forms for $\bar{\rho}_e/\bar{\rho}_c$. The exponential fit for $\gamma < 0$, however, unlike the linear fit, gives the physically appealing limit of $\bar{\rho}_e/\bar{\rho}_c$ vanishing asymptotically for long projections.

TABLE 4 Membrane fragmentation data used in calculating the average hydrodynamic gap between pipette wall and projection

L/R_p	L_{ves}/R_p	$2R_p$ (μm)	u (μm/s)	ϕ*	h (nm)
10	1 to 2	1.2 to 1.6	0.26	0.05 to 0.5	11 to 19
14	2 to 4	0.9 to 1.1	0.12	0.05 to 0.5	8 to 11
10.6	5.4	0.6 to 0.7	0.33	0.05 to 0.5	9 to 10

*Estimated range is consistent with backflow of Fig. 8.

length of the projection (Fig. 6). Enrichment at the projection's tip was also found with glycophorin C on the surface of the red cells deficient in protein 4.1 (Discher et al., 1994); this contrasted with the glycophorin C on normal cells, which exhibited a gradient very close to that of actin (Table 3). It may be noted that initial FRAP measurements of IgG-labeled glycophorin C ($\sim 10^3/\mu m^2$) on normal cell membranes indicate a connectivity to the skeleton, for this transmembrane protein, similar to that of Band 3 (Knowles, 1992). Importantly, these results with glycophorin C on normal versus protein 4.1-deficient membranes were found with bivalent IgG as well as monovalent Fab and thus eliminate the possibility of artifactual cross-linking. Other than the tabulated difference for the glycophorin C on the 4.1-deficient cells, no other constituent responses on these pathological cells appeared anomalous.

Measures of the pipette-membrane gap

Issues of 1) friction or adhesion between the pipette and membrane and 2) flow between the pipette wall and cell surface (Fig. 1) have long been recognized (Evans and Skalak, 1980). Integrations of the various FIMD-determined density fields were already presented as evidence against friction between the membrane and the pipette having a significant effect on the distribution of membrane components. To further characterize the gap between the membrane and pipette, inert fluorescent probes (dextrans) of several molecular weights were used as tracer particles in the bulk flow through the gap. In a first series of experiments, the pipette was plugged with an aspirated cell (~ 20 kdyn/cm^2), and this "presealed" pipette was translated into a surrounding solution of two different molecular weight dextrans having different fluorescent labels. After several minutes, the pipette with the cell still aspirated was translated out of this labeling zone, and the amount of each fluorophore in the pipette was quantitated. For normalization, the pipette was later filled with dextrans. This method of calibrating the fluorescence intensity ratios gave a measure of the sieving or filtration efficiency of various molecular weight dextrans relative to a 3-kDa dextran (Fig. 8 *A*). A dextran of 10 kDa convects through the gap formed between the pipette and membrane almost as efficiently as the 3-kDa dextran, whereas a molecule about the size of an antibody ($R_s \approx 5.2$ nm) will convect through the entire gap with a nominal frequency of success of ~ 0.25.

An effective hydrodynamic gap height, h, of order 10 nm was determined by following the translation of a membrane vesicle up a pipette prefilled with fluorescent dextrans (Fig. 8 *B*). The 3-kDa dextran was efficiently transported back behind the translating vesicle (nonfluorescing black spot), and the 500-kDa dextran tracer was simply pushed ahead of the fragment. An analysis of the flow mechanics in vesiculation is consistent with these results (Table 4 and Appendix 2) and has been described previously in terms of an elasticohydrodynamic instability (Kozlov et al., 1988). The average gap height for the hydrodynamics is an upper bound on the minimum gap that should be more directly related to the sieving efficiency of Fig. 8 *A*. This average gap may, in places, include a portion if not all of the hydration layer that is above the outer leaflet of lipid and is estimated at $\sim$10-16 nm, based on both the dimensions of cell surface proteins and carbohydrates and very limited information on molecular conformation (Viitala and Jarnefelt, 1985). Thus the pipette wall (with its "lubricating" layer of adsorbed albumin; ref. Markle et al., 1983) could, in some regions, be in intimate contact with the exoface of the cell (aspirated to $\Delta p = 20$ kdyn/cm^2). Some likely zones and forces of contact between the pipette and membrane are clarified in Appendix 3.

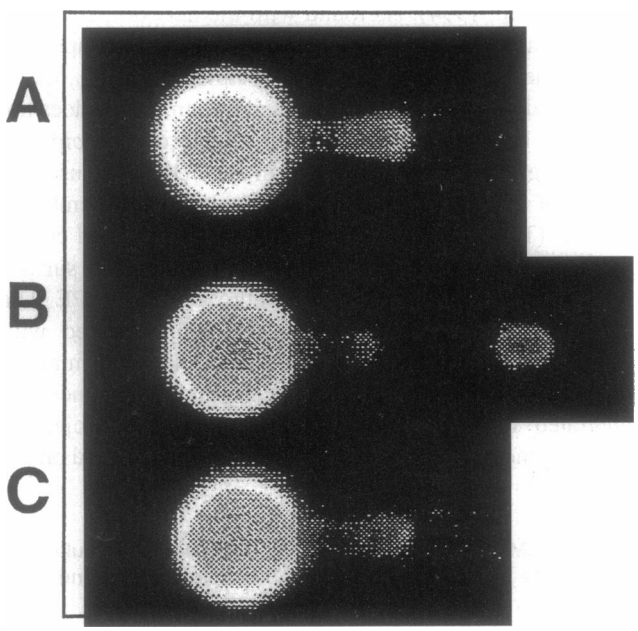

FIGURE 9 (*A*) Anti-FL-PE IgG bound to prelabeled FL-PE per the transfer technique of Fig. 4. The distribution appeared within $\sim$2 min of incubation with IgG and remained static for $\sim$5 min. (*B*) Subsequently, the tip of the aspirated projection was forced to vesiculate, and the vesicle began to convect up the pipette. (*C*) After a further $\sim$15 min, enrichment of IgG at the cap was again apparent.

Vesiculation

In a transfer experiment similar in procedure to the previous lipid diffusion measurements, cells uniformly prelabeled with FL-PE were first aspirated and then incubated with the anti-FL IgG. This assembled analog of an unconnected integral protein appeared highly enriched at the cap of the aspirated projection (Fig. 9) within just 2–3 min of the start of incubation. This end point of the evolution occurred much faster than the measured lipid diffusion (Fig. 4). This is clearly due to molecular transport by convection (Q_{ent} in Fig. 1) through the fluid gap between pipette and projection. FL-PE vesicles, which readily labeled the spherical portion of membrane outside the pipette (Fig. 4), are apparently too

large to convect into the gap. By vesiculating the IgG-labeled tip of the aspirated projection, it was further demonstrated that the membrane fragment is enriched in lipid-linked antibody. Approximately 15 min after vesiculation, some enrichment was again apparent at the cap of the remnant projection, suggestive of at least limited molecular motion.

The enrichment of an unconnected integral membrane protein on the vesicle and depletion of both network and connected integral proteins in the vesicle are fully consistent with the respective static gradients (Fig. 2). Importantly, these distributions are also consistent with "test-tube" methods: calcium-induced vesiculation and a number of other procedures, including storage of blood, all produce membrane vesicles enriched two- to threefold in GPI-linked proteins (Hagelberg and Allan, 1990). This occurs with the complementary depletion of skeletal proteins, Band 3, and glycophorin A. In addition, sickle cell membranes are known to vesiculate, and CD59 is found to be slightly reduced on sickle cells (Test and Woolworth, 1994). Agreement between the various vesiculation methods serves to validate FIMD. None of the other, more "traditional" methods, however, are able to examine single cells with the resolution and control over collective motions that are intrinsic to FIMD.

DISCUSSION AND ANALYSES

Observations of laterally mobile membrane receptors in the early 1970s provided some of the first clear evidence of membrane fluidity (Frye and Edidin, 1970); demonstrations and analyses of reversible cell deformations at about the same time clearly indicated a solid-like component to, at least, the red cell's membrane (Fung and Tong, 1968; Hochmuth and Mohandas, 1972). The somewhat disparate views of membrane behavior were subsequently merged in a conceptual model of the membrane as a fluid-solid composite (Evans and Hochmuth, 1977). The FIMD results presented here refine such descriptions of the composite system.

Bilayer

Transient gradients in the lipid bilayer (Figs. 4) may be contrasted with stable gradients in the other membrane components (Figs. 2, *B* and *C*; 5 *C*; and 9). These other component gradients do not appear to significantly dissipate, even under stress, for periods of ≥30 min. Furthermore, not only do these lipid diffusion experiments reinforce the image calibration scheme used to map relative surface densities of nonlipid components, they also show that gradients in lipid are physically attainable, although they are not sustainable in time. This is consistent with the bilayer being a surface fluid.

Additionally, a diffusion constant estimated from the time course of lipid diffusion onto the projection may be compared to previously published lipid diffusion constants. As a surface diffusion process, the progression of lipid probe down the static projection of membrane is likely to obey the evolution equation $\partial_t c = D(r_i)\nabla^2 c$, where $D(r_i)$ is the surface diffusivity and $c = c(r_i,t)$ is the surface concentration of probe at a point on the membrane located by the position vector r_i. From the time-dependent increase in probe density at the cap of various length projections (Fig. 4 and Table 2), a simplistic estimate for a uniform D_{lipid} on the membrane can be made based on a one-dimensional diffusion process in a half-space, where $D \sim L^2/2t$, or on more rigorous treatments of the geometry (Berk et al., 1992), which yield $D \sim L^2/[(\pi/2)t]$. A simple calculation from the lengths of the projections and the estimated time constants yields $D_{lipid} = 1.0 \pm 0.3 \times 10^{-9}$ cm^2/s (Table 3). This is close to the range of 1.2–2.0 $\times 10^{-9}$ cm^2/s reported for PE (*N*-[7-nitro-2,1,3-benzoxadiazol-4-yl]-PE) under a variety of buffer conditions at 21°C (Golan et al., 1984). Given the observations of density gradients in integral membrane proteins, a more appropriate approach to the full nonlinear problem might allow for $D_{lipid} =\cdot D(r_i)$, because the surface diffusivity of at least one fluorescent PE analog has been shown to decrease by a factor of 4 when vesicles of RBC-extracted lipids were compared to intact RBC membranes (Golan et al., 1984), i.e., increased integral protein density increasingly hinders diffusion. Nonetheless, the FIMD and FRAP results show reasonable concurrence. The agreement again suggests, for FIMD, that the pipette entrance does not significantly impede lateral transport at the innermost level of the exoface.

Integral membrane proteins

In spite of the possible intricacies of interaction between Band 3 (with its large cytoplasmic domain) and the skeleton, it is nevertheless worth estimating a mobile fraction of Band 3 in the intact, nascent membrane. A more thorough analysis including steric effects is given in Appendix 4, but a simple and seemingly accurate treatment ignores sterics and assumes mobile Band 3 is distributed like the unconnected integral proteins (components with $\gamma < 0$ in Table 3), whereas immobile Band 3 has the same distribution as the network. If we identify the mobile fraction of Band 3 with f and denote the unconnected proteins with a subscript u, an appropriate superposition using either of the different empirical fits listed in Table 3 takes the form (in the $L/R_p = 0$ limit for the exponential fit)

$$(1-f) * [1 + \gamma_{actin}(L/R_p)] + f * [1 + \gamma_u(L/R_p)] = [1 + \gamma_{B3}(L/R_p)].$$

This expression should be appropriate for extrapolating back to the undeformed or nascent membrane. Substituting the various numerical values in Table 3, $f \cong 0.22$–0.31. This determination of mobile fraction is only slightly below the range of 0.3–0.4 for Band 3 in both lateral (Golan and Veatch, 1980; Tsuji and Ohnishi, 1986) and rotational (Tsuji et al., 1988) diffusion.

Although a high mobility of the unconnected integral membrane proteins would seem to preclude direct interactions with the membrane skeleton, molecular exclusion at the membrane is proposed here as the mechanism for mobile protein enrichment toward the cap. Indeed, about 70% of the glycocalyx is associated with connected integral proteins, principally Band 3 and glycophorin A (Viitala and Jarnefelt, 1985). The transmembrane protein glycophorin A has been suggested to be in association with Band 3 (Nigg et al., 1980); certainly the transmembrane protein glycophorin C appears connected to the skeleton on normal cells. By direct connection or steric interaction with the underlying skeleton and as a consequence of the network's intrinsic elastic properties, a large fraction of these bulky, connected integral proteins end up enriched at the micropipette's entrance. The attached carbohydrates on both Band 3 and the glycophorins and the protein volumes both within and protruding above the outer leaflet would tend to squeeze out low-density mobile integral proteins like CD59 (~300 molecules/μm^2; Test and Woolworth, 1994), driving them toward the projection's cap (Fig. 10). The picture here is that of a forest of integral proteins rooted in a compressible network, and, within the forest, scurrying about in thermal motion are the "sheep-like," mobile integral proteins. When the intrinsic elasticity of the network leads to a condensation in some surface region as a result of cell deformation, the forest also condenses in that region and thereby displaces the "sheep" into more open spaces.

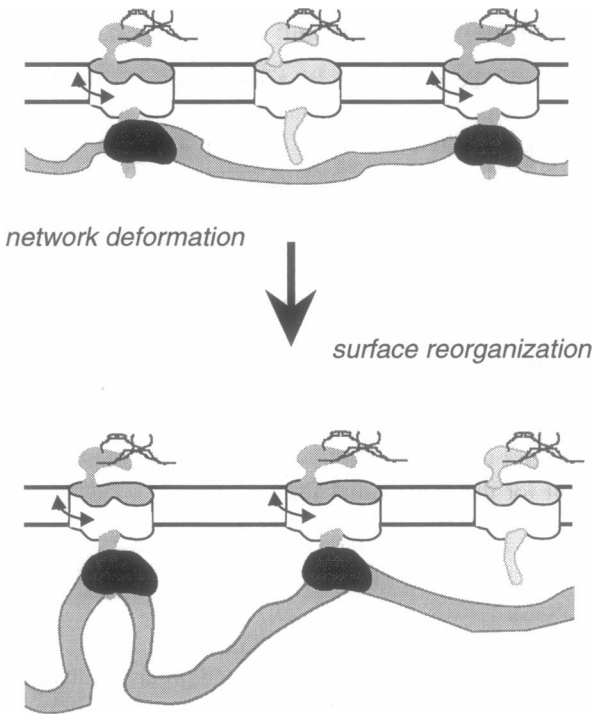

FIGURE 10 Highly schematic view of membrane component reorganization as a result of network deformation. The network-connected transmembrane proteins are pictured as asymmetric, thermally rotating structures.

Excluded surface area is not of necessity the only mechanism capable of contributing to the cap enrichment of unconnected integral membrane proteins. As the cap is the area of greatest mean curvature ($2/R_p$) along the projection, membrane curvature might be deemed important. However, mean curvature differs by a factor of exactly 2 between the cap and projected cylinder, regardless of the projection length L/R_p, and the change in membrane curvature is essentially a step function in z' ($1/R_p$ for $z' > R_p$). These features are not reflected in the experimental results, which show smooth gradients that increase with projection length. The proposed excluded volume mechanism therefore seems more consistent.

By equating the chemical potential at the cap and pipette entrance for any one of the unconnected integral proteins, the fits of Table 3 permit a simple estimate of the pertinent excluding area on a nascent red cell's exoface (see Appendix 4 for details): between 29% and 42% of the nascent or flaccid red cell's surface (fraction of S_2 in union with a fraction of S_3 in Fig. 1) appears to be occupied by network-connected proteins like Band 3. On rat basophillic leukemia cells (Ryan et al., 1988), for comparison, the obstacles to cell surface electrophoresis were estimated to range from 30 ± 15% to 77 ± 31% of total area for, respectively, the IgE receptor and ConA-labeled glycoproteins. A clear implication of the above estimate is that network condensation (e.g., $\bar{\rho}_e$) should be limited by the bulky, skeleton-connected integral proteins to a range below $\bar{\rho} \approx 2.4$–3. Consistent with this estimated maximum for network density, the measured values of $\bar{\rho}_e$ for the network did not exceed ~2 (Fig. 5 *A*). Furthermore, recent structural studies on the intramembrane domain of the Band 3 dimer (Wang et al., 1994) have shown it to be a bulky asymmetric molecule (approximately 10 nm by 3 nm) which, when rotating (as measured in rotational diffusion studies) and upon considering its high surface density (~$10^4/\mu m^2$) and the effect of boundary lipids, could dynamically sweep out an area of almost 30% within S_2. This would tend to exclude proteins, even those with lipid tails such as CD59, without affecting more mobile lipids. Band 3's extracellular domain in S_3 should add to this effect, and so should the glycophorins. In sum, the cap enrichment of the unconnected integral proteins such as CD59 appears to be consistent with an excluded volume that is coupled to the network. The intrinsic compressibility of the skeletal network may therefore be viewed as a primary cause of cell surface repatterning.

Network

Spectrin, actin, and protein 4.1 move collectively as an integrated structural unit distinct from other membrane components. The deformed state of the network in aspira tion, as defined by the underlying density gradient, appears static for periods of at least half an hour and was obtainable after cycles of rapid aspiration (Fig. 5 *C*). Clearly, the structure is more stable than labile: the physical response of

a density gradient appears to be independent of the inter-protein bonding holding the network together. The results here suggest, then, a tightly bonded spectrin-actin-4.1 network, consistent with both the stability of detergent-extracted membrane shells (Schmidt et al., 1993) and the organizational integrity maintained in specimens prepared for ultrastructural analysis (Byers and Branton, 1985). In contrast, however, to detergent treatments and electron microscopy, which can both be rather destructive in their reductionism, FIMD allows a direct visualization of the mechanically controlled reorganization of the network (Fig. 2 *B*) from its fairly homogeneous distribution in an intact membrane.

Large relative motions of the network and bilayer occur as the tensed bilayer flows over the stretched skeletal network. Contact between these two surfaces is presumably maintained, however, by the connecting linkages with the bilayer-embedded receptors such as Band 3. The network, bilayer, and integral membrane proteins all display the same projected shape; most notable in double-labeled cells is the near-superposability of the hemispherical caps at the tips of the projections. Thus, interlamina contact must be maintained to within optical resolution (~250 nm). Normal loads on the network, transmitted through the linkage proteins, are therefore the most readily postulated forces on the network. Tangential tractions on the network due to the fluid bilayer should only occur during the interval of relative motions of aspiration and not while the cell is held stationary in the pipette. Furthermore, tractions other than the normal tractions on the projected network seem minimal because of 1) the measurable gap between the cell and pipette (Fig. 8 and Table 4) and 2) the lines of evidence against obstruction of membrane components in entering the micropipette.

If, as was proposed from the outset, the stress response to the force of aspiration is primarily taken up by the nearly incompressible bilayer, then the highly elastic network may be viewed as merely conforming to the tensed lipid capsule. Deforming the network may therefore be likened to pushing a finger into a rubber sheet. Under a distribution of primarily normal loads on the sheet's surface, the sheet material thins at the fingertip and wrinkles or condenses at the base of the finger when constricted there. For the network, condensation at the pipette entrance is constrained to a molecularly thin layer by linkage proteins, and this occurs without microscopic wrinkling. Like the network, though, the graded response of the rubber sheet is sustained as long as the projection is held in place. The cumulated evidence is thus consistent with a simplified mechanical treatment of the red cell membrane composite in which the network is treated as a separate structure, elastic in nature. Its axisymmetric density field may then be fully utilized in providing a picture of the material's stretching.

Local expressions for the conservation of mass (Naghdi, 1972) have integral counterparts that may be fruitfully applied to the aspiration problem to calculate the stretches along the projection from the density field data. In projecting out an initially flat disk of radius R_D, conservation of mass gives ${}_{proj}\int \bar{\rho}_{net}\, da = {}_{disk}\int dA = \pi R_D{}^2$. Hence, $\pi R_D{}^2 = 2\pi R_p L$, or $R_D/R_p = (2L/R_p)^{1/2}$. The relative sizes of the pipette and starting disk give the stretch at the only material boundary in such an analysis: $\lambda_2(z = 0) = R_p/R_D = (2L/R_p)^{-1/2}$. Instead of a disk, for a uniform density initial configuration that is a portion of a spherical surface of radius R_o,

$$\lambda_2(z') = [r(z')/R_p]\left\{(R_o/R_p)^2 - \left[(R_o/R_p) - (1/R_o)\,{}_{pole}\int^{z'} \bar{\rho}_{net}\, dz'\right]^2\right\}^{-1/2},$$

where z' is the axial distance from the pole and the radial distance $r(z') = R_p$ for $z' \geq R_p$. Importantly, at the pole, $\lambda_1 = \lambda_2 = 1/\sqrt{\bar{\rho}_{net}}$. Deformation maps of a more general uniform-density initial surface, such as an ellipsoid, may also be calculated but can become increasingly unwieldy. It is clear, however, that there is little difference in the stretch fields calculated by starting with either a disk or a sphere.

Explicit illustrations of the stretching of material elements along the length of a projection of network are given in Fig. 11. At the very tip or cap, a small, initial patch of network is expanded without distortion. At the entrance, the initial patch has a large compressive "hoop" strain while also being highly elongated in the direction of aspiration: the material stretches in the two directions at an entrance point can easily differ by an order of magnitude. For the longer projections shown, the maximum stretch is about 85% of the maximum extension ($\lambda_{max} \approx 2.63$) for the spectrin filaments as calculated from both the reported contour length of ~200 nm and the in situ end-to-end length of ~76 nm (Byers and Branton, 1985). Moreover, for the longest projections studied here, the minimum relative surface density at the cap (Fig. 5 *A*) exceeds by at least 50% the minimum expected for an intact network $\bar{\rho}_{min} = (1/\lambda_{max})^2 \approx 0.14$. Indeed, the maximum stretch of the network on the aspirated projection often occurs near the pipette entrance rather than at the tip of the cap. Tremendous resilience of the red cell network in distortion is thus clearly manifested in many locations. Equally important, reasonable numerical characteristics of the stretch fields point to the overall consistency of the density field determinations.

CONCLUSIONS

FIMD has shown that one of the original characterizations of the red cell membrane as a multilayered fluid-solid composite (Evans and Hochmuth, 1977) is still very appropriate. Molecular heterogeneity has come to supplement this picture, and the simple analyses here have attempted to quantify, justify, and interrelate some of the kinematic differences. From these analyses, compressibility of the underlying skeletal network emerges as a key feature in the

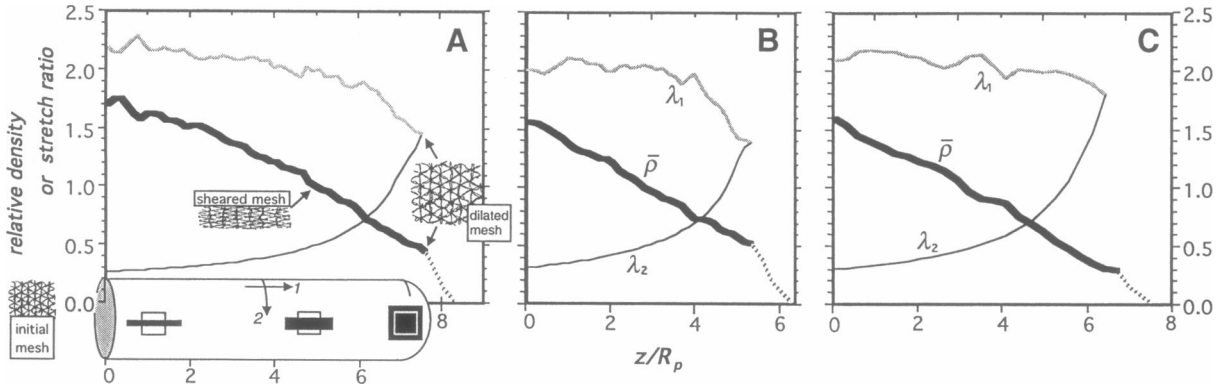

FIGURE 11 Stretching of the network in the aspirated projection. Experimentally determined relative surface density profiles (heavy lines) were integrated over the axisymmetric shape to give the material stretches along the indicated lines of principal curvature. The horizontal axis in *A* explicitly illustrates the stretch of an initially square piece of membrane as a function of position along the projection. Density gradients were reported with actin-labeling (*A* and *C*) or the anti-spectrin (*B*) antibody.

deformation-induced repatterning of many other membrane components.

APPENDIX 1

Define a surface coordinate ξ along a meridian on the projection, with $\xi = 0$ at the tip $z' = 0$ of the projection (Fig. 1) and $\xi = \pi R_p/2$ at the intersection of the cap and cylinder, where $z' = R_p$. If ρ is the mass per area of lipid, say, on the membrane, then the line density along the symmetry axis of the membrane is $\tilde{\lambda} = 2\pi R_p\rho$. An increment of mass for the cylinder is $dm = \tilde{\lambda}\, dz' = 2\pi R_p\rho\, d\xi$. An increment of mass for the cap would be $dm = \tilde{\lambda}\, dz' = 2\pi R(\xi)\rho\, d\xi/\sin(\xi/R_p)$, where $R(\xi) = R_p \sin(\xi/R_p)$ is the radial distance from the point ξ on the membrane to $z' = R_p[1 - \cos(\xi/R_p)]$. Thus, for both the cap and cylinder, an increment of mass has the same form $dm = \tilde{\lambda}\, dz' = 2\pi R_p\, \rho\, d\xi$. Hence, the difference in geometry between the cap and cylinder is properly taken care of, in principle, by integrating across a membrane projection's diameter to get the line density.

APPENDIX 2

The cell stuck at the entrance forms an annular gap that admits fluid; the fragment translates away from this with a similar separation distance from the wall, because a 3-kDa but not a 500-kDa dextran leaks back. One of the simplest annulus and plug models of the fragmentation process involves relating the flows past each object to the pressure drops across each object when the axisymmetric gap between the wall and each object is a uniform constant h. In this case, the lubrication equations (Probstein, 1989) appropriate to the translating plug reduce to

$$Q_{lkbk} = [\pi 2R_p\, \Delta P_{ves}]h^3/[12\eta L_{ves}] + uh\pi R_p\,,$$

where ΔP_{ves} and L_{ves} are the pressure drop across the plug and the length of the plug, respectively, and η is the fluid viscosity, which is assumed to be that of water, 1 mPa-s. With the quantities defined in the text, this can be rewritten in terms of the fraction of fluid volume, ϕ, between vesicle and cell that is contributed by the leakback:

$$\Delta P_{ves}[2R_p h^3]/[12\eta L_{ves}] = (u2R_p^2)[(1 - \phi)/2 - h/2R_p].$$

Based on the leakback of dextran and as summarized in Table 4, it appears that $(1 - \phi) \gg h/R_p$. The equation then simplifies to the same form as planar Pouseille flow, which is also a description of the flow through the stationary annular gap. Hence, if L_{proj} is the projection length of the still aspirated cell creating the annular flow, then

$$\Delta P_{tot} = \Delta P_{ves} + \Delta P_{proj}$$

$$= [u\eta/2R_p][3(2R_p/h)^3][(L_{proj}/2R_p)(1 - \phi) + (L_{ves}/2R_p)\phi],$$

where all quantities except h are measured or can be reasonably estimated.

Translation of the vesiculated fragment up the pipette was measured as a velocity u. The pipette entrance, although still plugged by most of the aspirated cell, allowed in a volume fraction ϕ of the fluid filling the space between the cell and fragment. This volume fraction could change with fragment position in the slightly tapered pipette, but it can be approximated from the measured dilution of the 3-kDa dextran's fluorescence. The total flow rate into this space, $Q_{tot} = u(\pi/4)(2R_p)^2$, thus arises from a flow through the entrance gap, $Q_{ent} = \phi Q_{tot}$, and a leakback flow past the fragment, $Q_{lkbk} = (1 - \phi)Q_{tot}$. When the gap surrounding the projection and the cell fragment within the pipette are modeled simply as an annulus at the entrance and a translating cylindrical plug, the two flow rates, Q_{ent} and Q_{lkbk}, can be added together, along with the pressure drops, to match both the measured Q_{tot} and the fixed ΔP. An average gap height assumed applicable to both fragment and cell body is then calculated to be in the range of 8–19 nm (Table 4).

APPENDIX 3

Normal tractions on the membrane cylinder can be calculated from a static equilibrium mechanical analysis of the axisymmetric cell configuration as sketched in Fig. 1. Given the uniform tension, T, in the bilayer, the balance equation at every point of a static bilayer in the direction normal to the surface is

$$T(1/R_1 + 1/R_2) = \sigma,$$

where R_α are the principal radii of surface curvature at the point. The load σ maintains the surface in the given shape. On the cap, both radii (or curvatures) are equal (hence the law of Laplace), and T can be calculated as in the text, $T = \Delta P D_s R_p/(D_s - 2R_p)$, where $\Delta P = P_{chamber} - P_{pip}$. Furthermore, on the cylindrical projection as a developable surface, one of the curvatures vanishes and the other is equal to the pipette radius; hence the normal load on the cylinder is

$$\sigma_{cyl} = T/R_p = \Delta P\, D_s/(2D_s - 4R_p).$$

An integrated balance on the cell in the direction parallel to the pipette axis identifies a balancing resultant force F, which keeps the cell from being drawn completely into the pipette:

$$(P_{cell} - \Delta P)\pi R_p^2 + F = P_{cell}\pi R_p^2 \Rightarrow F = \Delta P(\pi R_p^2).$$

If one accounts for the annular flow of Appendix 2, a frictional stress, τ_w, on the projection tends to pull the cell into the pipette with magnitude $F_{fr} = \tau_w \pi DL = \pi h R_p \Delta P$. However, $h \ll R_p$ implies that this frictional force is negligible, consistent with a negligible tension difference between the cap and the sphere. The balancing force F therefore arises from "contact" with the pipette entrance; this force is distributed over an annular face at the entrance. The area of this face is $\sim 2\pi R_p t$, with t less than or equal to the pipette wall thickness. Thus the load normal to this annular strip at the entrance is

$$\sigma_{ent} = \Delta P(\pi R_p^2)/(2\pi R_p t) = \Delta P * (R_p/2t),$$

at least of order ΔP. Because $D_s/2R_p \approx 3 \pm 1$ and most pipettes had $R_p/t > 4$–5, the ratio

$$\sigma_{ent}/\sigma_{cyl} = (R_p/t)\,[1 - 2R_p/D_s] > 1.$$

This implies that steric effects at the exoface arising from contact with the glass, should they exist, will be most prominent in the annular strip of membrane at the entrance face to the pipette. It is clear, however, that such forces at the pipette entrance have not significantly impeded material motions during aspiration: the cumulative amount of either actin, CD59, or antibody on the projection is not detectably different from the amount on a comparable area of undeformed membrane.

APPENDIX 4

Define ϑ as the areal fraction of network-connected integral proteins at the cap. This areal fraction should be viewed as having contributions from both surfaces S_2 and S_3. As a prime example, this includes immobile Band 3's intramembrane domain, together with its extracellular domain. Then for a given projection length $Z = L/R_p$, we note $\vartheta = \vartheta(Z)$. Let the ratio of entrance to cap densities of the network (Table 3) be $\chi_N(Z) = (\bar{\rho}_e/\bar{\rho}_c)_{Net}$. At the entrance and cap, the fractional area, Σ, of membrane surface accessible to the unconnected integral proteins like CD59 is, respectively,

$$\Sigma_e = 1 - \chi_N \vartheta$$

$$\Sigma_c = 1 - \vartheta.$$

Because the deformation responses appear the same whether aspiration is done within 100 ms or over a period 100 times longer, we assume that the aspiration process involves working through a number of equilibrium states. As such, the chemical potential of CD59-type molecules may be equated along the entire projection and, in particular, at the cap and the entrance. The chemical potential of these molecules may be different on the sphere versus the projection, but a balance over just the projection is consistent with the average ratio of CD59 to lipid on the aspirated projection being the same as on the spherical portion (cf. Fig. 6).

Denoting the surface densities of CD59 and other such unconnected molecules at the entrance and cap as $\rho_{e,U}$ and $\rho_{c,U}$, and then equating the chemical potential at these two points gives

$$\Gamma_e\, \rho_{e,U}/\Sigma_e = \Gamma_c\, \rho_{c,U}/\Sigma_c,$$

where Γ_e and Γ_c can, in general, be distinct surface activity coefficients. Combining expressions while writing $\chi_U = \rho_{e,U}/\rho_{c,U} = (\bar{\rho}_e/\bar{\rho}_c)_U$ and $\Gamma = \Gamma_e/\Gamma_c$:

$$\vartheta = (1 - \Gamma\chi_U)/(\chi_N - \Gamma\chi_U).$$

Using the curve fits of Table 3, assuming $\Gamma = 1$, and extrapolating from the aspirated configurations to the unaspirated configuration (i.e., $Z \to 0$) gives $\vartheta = 29$–42%. This is the estimated areal fraction of "skeleton"-immobilized, excluded volume on the exoface of a flaccid red cell. Furthermore, a portion of this exclusion reflects packing limitations on the surface; only $\sim 90\%$ of a surface can be covered by equidiameter discs, for example.

A very similar analysis can be applied under the consideration that both mobile and immobile Band 3 molecules act to exclude unconnected integral proteins. Replacing χ_N with χ_{B3}, one calculates $\vartheta_{tot\ B3} = 40$–54%. The areal fraction calculated previously should be denoted, in this context, as $\vartheta_{immobile\ B3}$. The mobile fraction of Band 3 is therefore taken to be

$$f = [\vartheta_{tot\ B3} - \vartheta_{immobile\ B3}]/\vartheta_{tot\ B3} = 22\text{–}28\%,$$

consistent with the estimate of f in the text.

We are grateful for antibody contributions from Dr. S. Marchesi (Yale University, New Haven, CT; polyclonal IgGs to the α-II(46) domain of α-spectrin) and from Dr. D. Anstee (Bristol, England; monoclonal IgGs designated BRAC-18 and BRIC-10). We are grateful for the cooperation of Dr. Sam Test (Children's Hospital, Oakland, CA) in the labeling of cells with rhodamine-tagged monoclonal antibody fragment against CD59. We are grateful for the pathological cells provided through the efforts of Dr. G. Tchernia (Hôpital Bicetre, Paris) and Professor P. S. Low (Purdue University, West Lafayette, IN). We gratefully acknowledge Evan A. Evans and Andrew Leung (University of British Columbia) for their initiation of fluorescence studies of red cell deformation. Professor Evans' analyses of and insights regarding FIMD were invaluable.

Supported in part by National Institutes of Health grants P01 DK32094-09 and R01 HL31579-13; by the National Science Foundation (DD) through U.S. Department of Energy Equipment Funds; by grants from the National Institutes of Health (NM); and by the Director, Office of Health and Environmental Research, Division of the U.S. Department of Energy, under contract DE-AC03-76SF00098.

REFERENCES

Berk, D. A., A. C. Clark, and R. M. Hochmuth. 1992. Analysis of lateral diffusion from a spherical cell surface to a tubular projection. *Biophys. J.* 61:1–8.

Byers, T. J., and D. Branton. 1985. Visualization of the protein associations in the erythrocyte membrane skeleton. *Proc. Natl. Acad. Sci. USA.* 82:6153–6157.

Debreuil, R., T. J. Byers, D. Branton, L. S. Goldstein, and D. P. Kiehart. 1987. Drosophila spectrin. I. Characterization of the purified protein. *J. Cell Biol.* 105:2095–2102.

Discher, D. E., N. Mohandas, and E. A. Evans. 1994. Molecular maps of red cell deformation: hidden elasticity and in situ connectivity. *Science.* 266:1032–1035.

Discher, D. E., R. Winardi, P. O. Schischmanoff, M. Parra, J. G. Conboy, and N. Mohandas. 1995. Mechanochemistry of protein 4.1's spectrin-actin binding domain: ternary complex interactions, membrane binding, network integration, structural strengthening. *J. Cell Biol.* 130:897–907.

Evans, E. A. 1989. Structure and deformation properties of red blood cells: concept and quantitative methods. *Methods Enzymol.* 173:3–35.

Evans, E. A., and R. M. Hochmuth. 1977. A solid-liquid composite model of the red cell membrane. *J. Membr. Biol.* 30:351–362.

Evans, E. A., and R. Skalak. 1980. Mechanics and Thermodynamics of Biomembranes. CRC Publications, Grand Rapids, MI.

Frye, L. D., and M. Edidin. 1970. The rapid intermixing of cell surface antigens after formation of mouse-human heterokaryons. *J. Cell Sci.* 7:319–335.

Fung, Y. C. 1993. Biomechanics: Mechanical Properties of Living Tissues. Springer-Verlag, New York.

Fung, Y. C., and P. Tong. 1968. Theory of sphering of red blood cells. *Biophys. J.* 8:175–198.

Golan, D. E., M. R. Alecio, W. R. Veatch, and R. R. Rando. 1984. Lateral mobility of phospholipid and cholesterol in the human erythrocyte membrane: effects of protein-lipid interactions. *Biochemistry.* 23: 332–339.

Golan, D. E., and W. Veatch. 1980. Lateral mobility of band 3 in the human erythrocyte membrane studied by fluorescence recovery after photobleaching recovery. *Proc. Natl. Acad. Sci. USA.* 77:2537–2541.

Goodman, S. R., K. E. Krebs, C. F. Whitfield. B. M. Riederer, and I. S. Zagon. 1988. Spectrin and related molecules. *Crit. Rev. Biochem.* 23: 171–234.

Hagelberg, C., and D. Allan. 1990. Restricted diffusion of integral membrane proteins and polyphosphoinositides leads to their depletion in microvesicles released from human erythrocytes. *Biochem. J.* 271: 831–834.

Hiraoka, Y., J. W. Sedat, and D. A. Agard. 1987. The use of a charge-coupled device for quantitative optical microscopy of biological structures. *Science.* 238:36–41.

Hochmuth, R. M. 1987. Properties of red bood cells. *In* The Handbook of Bioengineering. R. Skalak and S. Chien, editors. McGraw-Hill, New York.

Hochmuth, R. M., and N. Mohandas. 1972. Uniaxial loading of the red cell membrane. *J. Biomech.* 5:501–509.

Katnik, C., and R. Waugh. 1990. Alterations of the apparent expansivity modulus of red blood cell membrane by electric fields. *Biophys. J.* 57:877–882.

Knowles, D. 1992. Ph.D. thesis. University of British Columbia.

Kozlov, M. M., D. Lerche, and W. Meier. 1988. RBC membrane instability for large pipette deformation—a theoretical approach. *Biorheology.* 25: 843–856.

Kozlov, M. M., and V. S. Markin. 1990. Model of red blood cell membrane skeleton. *In* Contemporary Problems of Biomechanics. G. G. Chernyi and S. A. Regirer, editors. CRC Press, Boca Raton, FL. 11–54.

Laurent, T. C., and K. Granath. 1967. Fractionation of dextran and ficoll by chromotagraphy on Sephadex G-200. *Biochim. Biophys. Acta.* 136: 191–198.

Markle, D. R., E. A. Evans, and R. M. Hochmuth. 1983. Force relaxation and permanent deformation of erythrocyte membrane. *Biophys. J.* 42: 91–98.

Mohandas, N., and E. A. Evans. 1994. Mechanical Properties of the red cell membrane in relation to molecular structure and genetic defects. *Annu. Rev. Biophys. Biomol. Struct.* 23:787–818.

Mohandas, N., R. Winardi, D. Knowles, A. Leung, M. Parra, E. George, J. Conboy, and J. Chasis. 1992. Molecular basis for membrane rigidity of hereditary ovalocytosis—a novel mechanism involving the cytoplasmic domain of band 3. *J. Clin. Invest.* 89:686–692.

Moriyama, R., H. Ideguchi, C. R. Lombardo, H. M. Van Dort, and P. S. Low. 1992. Structural and functional characterization of band 3 from southeast asian ovalocytes. *J. Biol. Chem.* 267:25792–25797.

Naghdi, P. M. 1972. The theory of shells and plates. *In* S. Flugge's Handbuch der Physik, Vol. VIa/2. C. Truesdell, editor. 425.

Naghdi, P. M., and L. Vongsarnpigoon. 1985. Some general results in the kinematics axisymmetrical deformation of shells of revolution. *Q. Appl. Math.* 43:23–36.

Nakashima, K., and E. Beutler. 1978. Effect of anti-spectrin antibody and ATP on deformability of resealed erythrocyte membranes. *Proc. Natl. Acad. Sci. USA.* 75:3823–3825.

Nigg, E. A., C. Bron, M. Girardet, and R. J. Cherry. 1980. Band 3-glycophorin A association in erythrocyte membrane demonstrated by combining protein diffusion measurements with antibody-induced cross-linking. *Biochemistry.* 19:1887–1893.

Noda, M., K. Yoon, G. A. Rodan, and D. E. Koppel. 1987. High lateral mobility of endogenous and transfected alkaline phosphatase: a phosphatidylinositol-anchored membrane protein. *J. Cell Biol.* 105: 1671–1677.

Probstein, R. F. 1989. Physicochemical Hydrodynamics. Butterworths, Stoneham, MA.

Ryan, T. A., J. Myers, D. Holowka, B. Baird, and W. W. Webb. 1988. Molecular crowding on the cell surface. *Science.* 235:61–64.

Schmidt, C. F., K. Svoboda, N. Lei, I. B. Petsche, L. E. Berman, C. R. Safinya, and G. S. Grest. 1993. Existence of a flat phase in red cell membrane skeletons. *Science.* 259:952–955.

Stokke, B. T., A. Mikkelson, and A. Elgsaeter. 1986. The human erythrocyte membrane may be an ionic gel. I. Membrane mechanochemical properties. *Eur. Biophys. J.* 13:203–218.

Takakuwa, Y., G. Tchernia, M. Rossi, M. Benabadji, and N. Mohandas. 1986. Restoration of normal membrane stability to unstable protein 4.1-deficient erythrocyte membranes by incorporation of purified protein 4.1. *J. Clin. Invest.* 78:80–85.

Test, S., and V. S. Woolworth. 1994. Defective regulation of complement by the sickle erythrocyte: evidence for a defect in control of membrane attack complex formation. *Blood.* 83:842–852.

Tsuji, A., K. Kawasaki, S. Ohnishi, H. Merkle, and A. Kusumi. 1988. Regulation of band 3 mobilities in erythrocyte ghost membranes by protein association and cytoskeletal meshwork. *Biochemistry.* 27: 7447–7452.

Tsuji, A., and S. Ohnishi. 1986. Restriction of the lateral motion of band 3 in the erythrocyte membrane by the cytoskeletal network: dependence on spectrin association state. *Biochemistry.* 25:6133–6139.

Viitala, J., and J. Jarnefelt. 1985. The red cell surface revisited. *Trends Biochem. Sci.* 10:392–395.

Wang, D. N., V. E. Sarabia, R. Reithmeier, and W. Kuehlbrandt. 1994. Three-dimensional map of the dimeric membrane domain of the human erythrocyte anion exchanger, band 3. *EMBO J.* 13:3230–3235.

Waugh, R. E. 1983. Effects of abnormal cytoskeletal structure on eythrocyte membrane mechanical properties. *Cell Motil.* 3:609–622.

Zhang, F., B. Crise, B. Su, Y. Hou, J. K. Rose, A. Bothwell, and K. Jacobson. 1991. Lateral diffusion of membrane-spanning and glycosylphosphatidyl-inositol-linked proteins: toward establishing rules governing the lateral mobility of membrane proteins. *J. Cell Biol.* 115: 75–84.